Holes in Optical Lightning Flashes: Identifying Poorly-Transmissive Clouds in Lightning Imager Data

Michael Peterson[1]

[1] ISR-2, Los Alamos National Laboratory, Los Alamos, New Mexico

Corresponding author: Michael Peterson (mpeterson@lanl.gov), B241, P.O. Box 1663 Los Alamos, NM, 87545

Key Points:

- Certain clouds block optical lightning emissions from reaching orbit, which can lead to missed detections
- Poorly-transmissive clouds modify the spatial energy distribution of large and bright optical pulses – in some cases creating holes
- We use such anomalies in the spatial radiance data to identify poorly-transmissive clouds in the lightning imager data

LA-UR-20-22888

Abstract

Space-based optical lightning sensors including the Lightning Imaging Sensor (LIS) and Geostationary Lightning Mapper (GLM) are pixelated imagers that detect lightning as transient increases in cloud-top illumination. Detection requires optical lightning emissions to escape the cloud-top to space with sufficient energy to trigger a pixel on the imaging array. Through scattering and absorption, certain clouds are able to block most light from reaching the instrument, causing a reduction in Detection Efficiency (DE).

We use cases of radiant lightning emissions that illuminate large cloud-top areas to examine scenarios where clouds block light in only certain pixels on the imaging array. In some cases, these anomalies in the spatial radiance distribution from the lightning pulse leads to "holes" in the optical lightning flash where certain pixels fail to trigger, entirely. Such holes are identified algorithmically in the Tropical Rainfall Measuring Mission (TRMM) satellite LIS record over the southern Continental United States, and the microphysical properties of the coincident storm region are queried. We find that holes primarily occur in tall (IR $T_b < 235$ K) convection (87%) and overhanging anvil clouds (10%). The remaining 3% of holes occur in moderate-to-weak convection or in clear air breaks between stormclouds.

We further demonstrate how an algorithm that assesses the spatial radiance patterns from energetic lightning pulses might be used to construct an optical transmission gridded stoplight product for GLM that could help operators identify clouds with a potentially-reduced DE.

Plain Language Summary

Lighting sensors on satellites detect lightning by looking at how they illuminate their surrounding thundercloud. Instruments like the Lightning Imaging Sensor (LIS) register lightning events by comparing high-speed movies of cloud-top brightness with the comparably steady-state background. However, there are some cases where the cloud is able to block the light produced by lightning from passing through. If too little energy makes it to the top of the cloud, the instrument will not be able to differentiate the light from lightning from the background and the lightning will not be detected.

In this study, we examine how clouds are illuminated by lightning to identify scenarios when light is blocked from reaching the LIS instrument. We compare "holes" in LIS measurements with the meteorological measurements from the other sensors on the Tropical Rainfall Measuring Mission (TRMM) satellite to understand what types of clouds can inhibit lightning detection. We find that it is not just the tall thunderclouds that are responsible for holes in optical flashes, but also overhanging anvil clouds, and even breaks in the clouds surrounding the thunderstorm. These insights might be used to construct a gridded stoplight product that can alert end users to issues with optical transmission.

1 Introduction

Recent analyses of Geostationary Lightning Mapper (GLM: Goodman et al., 2013; Rudlosky et al,. 2019) observations from NOAA's Geostationary Operational Environmental Satellites (GOES) have revealed that while GLM meets its required specifications for detection over 24 hours (Bateman and Mach, 2020), there are drastic reductions in DE in certain storms compared to ground-based radio-frequency lightning locating systems (i.e., Bitzer, 2019; Said and Murphy, 2019; Thomas, 2019; Rutledge et al., 2019). Differences in instrument performance between GLM and the ground networks has been attributed to detection physics. RF emissions from lightning escape the cloud unimpeded, while the optical emissions that GLM measures interact with the cloud medium through scattering and absorption. Computational models have shown how optical emissions are diluted in space and delayed in time as the result of scattering in various cloud geometries (Thomson and Krider, 1982; Koshak et al., 1994; Light et al., 2001a).

The clouds observed in nature are far more complex than in the models, however, and this adds a layer of complexity to how the optical lightning emissions recorded from space are distributed in time and space. The microsecond-scale scattering delay in the optical waveforms from lightning emissions compared to the RF signals from the same event has been measured from space (Suszcynsky et al., 2000; Light et al., 2001b). Comparisons between space-based optical lightning sensors and Very High Frequency (VHF)-band RF instruments have revealed that low-level light sources are poorly-detected from orbit, and that coincidence often begins late in the lightning flash – many milliseconds following the first RF pulse (Thomas et al., 2000).

While channel length (which increases as a function of time) is an important control on optical detection from space (Zhang and Cummins, 2020), coincident observations between a

lightning imager and a wideband photodiode detector have indicated that the footprint area of the illuminated cloud is primarily a function of event intensity (Suszcynsky et al., 2001). For this reason, the group illuminated area (and related number of events per group) have been used as "return stroke detectors" in lightning imager datasets (Koshak, 2010).

However, the shape of the group and how the optical radiance is distributed across its footprint is equally as important as the group size for understanding where the optical signals come from and how they interact with the clouds. We have previously demonstrated that the spatial distribution of group optical energy – referred to henceforth as the group radiance pattern – can be sculpted by the geometry of the complex cloud scene (Peterson et al., 2017a,b). Cases have been identified where the lightning emissions escape the side of the cloud and illuminate lower cloud decks, reflect off the sides of neighboring convective clouds, or are partially obscured in certain cloud regions. All of these features in the Lightning Imaging Sensor (Christian et al., 2000; Blakeslee et al., 2014) and now GLM measurements are evident in images of lightning taken by NASA's high altitude aircraft (Christian et al., 1983; 1987) and astronauts on the Space Shuttle (Vonnegut et al., 1985) and International Space Station (ISS). We also previously used GLM group radiance patterns to produce a lightning-based cloud imagery product (Peterson, 2019a).

In this study, we focus on the case where the optical energy at certain points in the group footprint is clearly suppressed compared to neighboring illuminated cloud regions. We propose that these anomalies in the group radiance pattern can be used to identify poorly-transmissive clouds using only the lightning imager data. A special case of this type of anomaly is when "holes" occur in the group footprint where no events are detected in a contiguous region on the imaging array that is completely surrounded by illuminated pixels. We will use holes in LIS

groups to identify cases of poorly-transmissive clouds, and assess their microphysical properties using the meteorological instrumentation on the Tropical Rainfall Measuring Mission (TRMM: Kummerow et al., 1998) satellite. We will then use all LIS group measurements from such a storm to develop an algorithm for identifying the general case of group radiance anomalies that do not, necessarily, produce holes. This prototype algorithm could be used in the future to generate a gridded GLM product to alert end users of cloud regions that may have a reduced GLM DE.

2 Data and Methodology

2.1 The Tropical Rainfall Measuring Mission (TRMM) Satellite

This study uses 16 years of coincident measurements from the instruments on the TRMM satellite to identify holes in LIS groups and describe the cloud regions responsible for them. In addition to LIS, the TRMM satellite featured a Precipitation Radar (PR), a Microwave Imager (TMI), and a Visible and Infrared Scanner (VIRS).

The TRMM sensor package is described at length in Kummerow et al. (1998), which we summarize in the remainder of this section. The TRMM PR was the first rain radar in space and provided reflectivity data across a 215-km wide swath with a 4.3 km horizontal and 0.25 km resolution (at nadir before, satellite boost in 2001). The PR was nominally sensitive down to rain rates of $\leq$ ~0.7 mm h^{-1}, though echoes below 15 dBZ corresponding to rain rates as low as 0.1 mm h^{-1} were routinely measured. In its normal observation mode, the PR antenna scans in the cross-track direction over its ±17° scan angle (which results in the narrowest swath of all TRMM

instruments) to fill in a three-dimensional grid of reflectivity data describing each storm below the satellite.

The TMI, meanwhile, provided passive microwave measurements in nine independent channels at six different center frequencies. Each of these channels had either a horizontal or vertical polarization. Combining the passive microwave brightness temperatures from the horizontal and vertical channels for a given central frequency - for example, 37 GHz (TMI channels 6 and 7), or 85 GHz (TMI channels 8 and 9) – corrects the passive microwave measurements (Polarization Corrected Temperatures – PCTs: Spencer, 1989; Toracinta et al., 2002; Cecil and Chronis, 2018) for differences in surface emissivity across the scene.

While the PR scanned in the cross-track direction, the TMI had a circular scan geometry whose beam viewed the Earth's surface 49° offset from nadir. The resulting TMI swath had an effective width of 759 km after launch, with pixels whose Effective Fields of View (EFOV) were 9.1 km in the cross-track direction at nadir for channels 1-7, and 4.1 km for channels 8-9 (the 85 GHz channels). Down-track EFOVs varied between the different central frequencies and ranged from 7.2 km (85 GHz) to 63.2 km (10 GHz).

The final TRMM instrument for probing storm structure, VIRS, was a 5-chanel imaging spectroradiometer. The central wavelengths of the VIRS channels matched NOAA's Advanced Very High Resolution Radiometer (AVHRR) instrument and included 0.623 μm (VIRS Channel 1, red band), 1.161 μm (VIRS Channel 2, mid infrared), and three thermal bands: 3.784 μm (VIRS Channel 3), 10.826 μm (VIRS Channel 4), and 12.028 μm (VIRS Channel 5). Like the PR, VIRS scanned in the cross-track direction, but over a wider 720 km swath with a ~4 km pixel resolution after launch.

154

155 2.2 The TRMM Lightning Instrument Sensor (LIS)

156

157 LIS is a staring imager that records optical radiance in a narrow band around the 777.4
158 nm neutral Oxygen emission line multiplet at a nominal frame rate of 500 Frames Per Second
159 (FPS) and triggers whenever the radiance in a pixel rises above the steady-state background
160 value during a single 2-ms integration frame (Christian et al., 2000). The LIS FOV was
161 approximately 600 km across, while nominal pixel sizes were ~3 km at nadir before the 2001
162 satellite boost and ~4.5 km afterwards. Thus, the LIS had a spatial domain similar to VIRS or the
163 TMI with a comparable spatial resolution to the VIRS or PR.

164 Single CCD pixel triggers are termed "events" in the LIS data nomenclature. Events are
165 clustered into features that describe lightning processes at various temporal scales (Christian et
166 al.,2000; Mach et al., 2007). Individual events are then clustered into "group" features that
167 approximate the illumination from a single optical lightning pulse. Groups are defined as
168 contiguous regions on the Charge Coupled Device (CCD) imaging array that simultaneously
169 produce events. This association is only an approximation because lightning can produce
170 multiple optical pulses within the 2-ms integration time for the instrument, while some optical
171 lightning pulses can last longer than 2-ms. Groups are further clustered into "flash" features that
172 approximate physically-distinct and complete lightning flashes, and are defined as collections of
173 groups in close space (5.5 km) and time (330 ms) proximity following the Weighted Euclidean
174 Distance (WED) model described in Mach et al. (2007). We further define "series" features that

describe periods of sustained illumination during the flash (Peterson and Rudlosky, 2018), while the LIS processing software defined "area" features that represent thunderstorm snapshots.

2.2.1 Identifying Holes in LIS Groups

The first LIS hole that we identified occurred in the example flash (Figure 1) from Peterson and Liu (2013). The hole was co-located with the tall and intense convective PR feature outlined in white in Figure 1b in that study. We were unaware of the hole at the time of publication, but its later discovery inspired us to find more examples of this phenomenon. To this end, we developed the following algorithm to identify arbitrary LIS holes.

The LIS event data includes the X and Y locations (0-127 in each dimension) of each illuminated pixel as well as the optical radiance measured during that event. We can thus report the spatial energy distribution during each LIS group by populating a 128x128 array with the measured radiances from each constituent event at their specified pixel X and Y locations. Two-dimensional arrays that always have the same dimensions are well-suited for automated image processing techniques. For our application of identifying holes in LIS groups, we simply perform a fill function on the outer portion of the array that is not part of the group, and then search the image for contiguous clusters of pixels that lack events.

This is essentially an inverse of the technique used to identify groups in Christian et al. (2000). As such, hole features contain child counts and information about the non-illuminated pixels. We also cross-link each hole to its "sibling" group feature, allowing us to inject hole features into the full LIS flash clustering hierarchy. There are two key differences between hole

196 features and groups, however. First, holes are defined using a stricter 4-neighbor search than the
197 8-neighbor search used with groups. Two non-illuminated pixels sharing corners with each other
198 will not be clustered into the same hole feature. Second, we cannot compute a radiance-weighted
199 centroid location for the hole feature because the measured radiance is always zero. Instead, we
200 report the hole location using the average latitude and longitude position. This procedure yielded
201 44,829 hole features over the LIS domain between 1/1/1998 and 9/21/2014.

202

203 2.2.2 Collocating LIS holes with PR/TMI/VIRS Measurements

204 In order to examine the properties of storm regions that produce LIS holes, we must
205 identify which PR, TMI, and VIRS pixels are co-located with the LIS hole feature. Initial
206 attempts at associating individual non-illuminated pixels with the other sensors were confounded
207 by strong gradients in the storm properties that often exist across the hole features. In some
208 instances, VIRS Channel 4 infrared brightness temperatures might be 190 K on one side of a
209 hole and 290 K on the other. Residual parallax, beam filling effects, and partial illumination of
210 LIS pixels make a pixel-to-pixel analysis unfeasible.

211 For this reason, we focus on the storm properties surrounding the hole centroid location.
212 For every hole feature, we collect all PR / VIRS / TMI 85 GHz pixels within a 5-km radius of the
213 hole centroid and all low-resolution TMI pixels (Channels 1-7) within 10-km, and then compute
214 standard Precipitation Feature (PF: Liu et al., 2008) products using these pixels. These include
215 the minimum 37 and 85 GHz PCT, the minimum VIRS CH4 IR T_b, the PR maximum heights of
216 15, 20, 30, an 40 dBZ, and the maximum near surface reflectivity and rain rate. Mean PR vertical
217 radar profiles are also computed for each hole feature.

2.2.3 LIS Gridded Products

The final LIS data that we consider are gridded products similar to the operational GLM grids produced by NOAA (Bruning et al., 2019). These grids expand the point measurements recorded by GLM / LIS to fill the spatial extent of optical lightning activity. For example, the grid that corresponds to flash rate, Flash Extent Density (FED: Lojou and Cummins, 2004), counts the number of times each unique gridpoint is illuminated by a different flash. Total Optical Energy (TOE), meanwhile, sums the reported radiance from all events that illuminate each gridpoint. Finally, Average Flash Area (AFA), computes the average illuminated area of all flashes that touch a given pixel. These grids are produced for every storm in our analysis domain that reports a LIS hole feature.

3 Results

Our analysis of LIS group radiance anomalies including holes is organized into three parts. First, we will identify and analyze a thunderstorm within the narrow PR swath that contains a LIS hole and that has sufficient lightning activity to generate multiple large (> 8 pixel) LIS groups. Next, we will analyze all large (3+ pixel) holes over our TRMM analysis domain and examine the PR, TMI, and VIRS measurements coincident with their centroids. Finally, will extend our analyses from holes to all types of group radiance anomalies where there are indications of diminished radiance making it to the space-based instrument. We will return to the thunderstorm case from the first section to develop a prototype algorithm for identifying general radiance anomalies and discuss the prospect of using this approach to create an optical

transmission stoplight product for GLM.

3.1 LIS Hole Case Study

A coastal TRMM thunderstorm that produced a large hole in a LIS group is identified over Mexico northwest of Mazatlán on 8/8/2011 at 02:26 UTC. A total of 53 large (>8 pixels) LIS groups that could have produced holes were identified while the instrument was in view of the storm. While only two of these groups contained holes, 10 others had highly-irregular footprints indicative of clouds blocking the optical emissions from reaching orbit. This abundance of non-hole radiance anomalies in LIS groups was the determining factor for selecting this case over the other features in our database.

The radiance patterns from the 12 groups with radiance anomalies are shown in Figure 1. The X and Y axes in each panel correspond to the X and Y pixel coordinate on the LIS CCD array, and each group is plotted as a greyscale image according to pixel radiance. The brightest event in each group shaded white while non-illumianted pixels are shaded black. Pixels that produced events further have a + symbol drawn at their centers, or a * symbol if the event at that pixel had the highest radiance in the group. The panels are organized in sequential time order, and their titles indicate the TAI93 time counter used by the LIS instrument at the time of the group.

While typical LIS groups have a bright pixel at the center of a quasi-concentric footprint, the groups in Figure 1 all deviate from this model by having asymmetrical footprints and dim or non-illuminated pixels close to the brightest events. Similarities in how the clouds are illuminated between panels – particularly in the locations of the brightest events and the non-

illuminated pixels – are due to these 12 groups describing repeated illumination of the same cloud region over a 77-s period, with differences in the radiance pattern resulting from the varying intensity of the optical source and its precise location within the thunderstorm. The change in x-position on the LIS CCD array from 123 in Figure 1a to 7 in Figure 1l is due to satellite motion and shows the thunderstorm passing through the LIS FOV.

Holes can be noted as contiguous regions of black pixels (lacking symbols) within the group footprints shown in Figure 1b and g. The remaining panels in the top two rows of Figure 1 nearly form holes, except no events are recorded along the western flanks of the groups. The key caveat of using holes to identify poorly-transmissive clouds is that they are only a special case of radiance anomalies in the LIS groups. The remaining groups in the top two rows of Figure 1 have their radiance blocked by the same cloud region that made the holes in Figures 1b and g, but the events do not form a closed region of interest that can be identified as a hole by our image processing algorithm. Moreover, the smaller (3-pixel) hole in Figure 1g is located adjacent to pixels with dim events that are surrounded on three sides by notably brighter pixels. This 170-pixel group is the largest recorded by LIS from this storm and its exceptional brightness allowed it to illuminate cloud regions that were dark in the other groups shown in Figure 1 (albeit with events near the minimum threshold for detection).

The poorly-transmissive cloud region responsible for the holes and other group radiance anomalies in Figure 1 also impacted the gridded products for the thunderstorm of interest. Figure 2 shows four grids that integrate all LIS data over the ~80 s viewtime. Figure 2a depicts the FED and has group centroid locations overlaid as red box symbols. This thunderstorm produced 15 flashes, in total, with most groups and the highest FEDs located in a convective feature in the eastern half of the overall illuminated cloud region bounded by FED > 0.

The storm core and the poorly-transmissive cloud region are most notable in the TOE grid in Figure 2b. TOE is calculated by summing the radiances of all LIS events that correspond to each gridpoint. The convective core of the storm has the greatest TOE values, while the hole manifests as 6 gridpoints just offshore from the costal storm core with very low TOE values compared to the surrounding gridpoints. This particular cloud region is thus able to block most of the light produced by lighting from reaching orbit – but it is occasionally illumianted. When these 6 gridpoints are illuminated, the AFA grid in Figure 2c indicates that it is by the larger flashes with illuminated footprint areas exceeding 1000 km^2. By contrast, the average flash sizes in the convective core are on the order of a few hundred square kilometers.

It is tempting to interpret AFA distributions like this with small flashes in convective regions and AFA increasing with radial distance from the storm core as evidence for the natural opposition between flash size and flash rate (Bruning and MacGorman, 2013) that partially explains why flashes are small in convective cells and large in electrified stratiform or anvil clouds. However, the AFA gridded product is not entirely appropriate for making such an assessment because it measures the extent of the cloud region that is illuminated by lightning and not the physical structure of lightning flashes. Extremely bright optical pulses can produce exceptionally-large groups like the example in Figure 1g that illuminate all nearby clouds at once – regardless of whether they contributed to the flash, or are even electrified. Such groups can reach 10,000 km^2 in area under the right conditions and these single bright groups completely define the footprint area of the flash that is used to construct the AFA grid. An alternate explanation for why AFA increases outward from convection is that flashes of all sizes illuminate the storm core, while only the brightest cases can illuminate the entire storm out to its periphery with enough optical energy in these distant pixels to trigger LIS or GLM.

Our case in Figure 2 supports the latter explanation. All of the group centroids (red boxes in Figure 1a) are located in mid-range AFA regions (blue – green) representing flashes < 2,000 km^2 in area. While the periphery of the storm and the non-transmissive cloud region have yellow and red pixels indicating very large flashes, there are no group centroids there to indicate lateral flash development into these regions. The fourth grid in Figure 2d provides another perspective by averaging the maximum event energy for every group that touches each gridpoint. Low values in the storm core indicate that it was illuminated by a larger proportion of dim flashes, overall, than surrounding regions. The flashes that illuminate the periphery regions and the hole all have at least one very bright event somewhere in their footprint. Thus, the flashes that illuminate these regions are large because they are bright enough to scatter energy across the scene at levels that LIS can detect. Cases like this are why we use group centroids (red boxes) rather than events to document lateral flash development (Peterson et al., 2018; Peterson, 2019b). Group centroid positions are less sensitive to the brightness of the optical pulse and the background radiance of the scene than the individual events.

We use the other TRMM instruments to examine the precipitation structure of this thunderstorm case in Figure 3. The map in Figure 3b shows the VIRS CH4 infrared brightness temperatures across the same spatial domain as Figure 2. The solid black lines transect the poorly-transmissive cloud region depicted in Figure 2. PR vertical reflectivity cross sections and VIRS CH4 brightness temperature traces are plotted for the quasi-meridional line in Figure 3a and for the quasi-zonal line in Figure 3c.

Perhaps the most notable aspect of Figure 3b is that the thunderstorm feature in the infrared imagery is considerably smaller than in the gridded lightning imagery in Figure 2. Lightning events extend outward from the primary thunderstorm feature (whose 15 dBZ echo

tops reached 17 km and minimum infrared brightness temperatures were below 185 K) to illuminate large swaths of the relatively-low cloud layer surrounding the storm core – even reaching as far as the eastern shore of the Ensenada de Pabellones to the northwest. While cloud tops remained below freezing in these boundary cloud regions, they largely lacked PR echoes.

The poorly-transmissive cloud region that produced the holes in Figure 1b and g was located immediately to the west of the storm core. The PR cross section in Figure 3a indicates that this region is an overhanging anvil cloud. The PR echoes that were observed in this region were centered in the upper part of the storm with a clear air gap between this upper layer and the surface. Even with sparse PR data across the anvil, the VIRS CH4 infrared brightness temperatures shows that it was a continuation of the cold cloud (< 235 K) feature that encompassed the storm core.

For this particular case, the optical lightning emissions were able to frequently illuminate the tall and intense convective core of the thunderstorm, but had difficulty penetrating the overhanging anvil immediately adjacent to it. Thus, poorly-transmissive clouds are scenario-specific and identifying them is not as simple as picking the most intense convection. Using convective intensity to warn on possible reductions in instrument DE would likely lead to frequent false alarms while missing important events like overhanging anvils.

3.2 Statistics of TMM Measurements in LIS Hole Features

In total, we identified 44,829 hole features across the LIS domain that have coincident thunderstorm measurements from the remaining TRMM instruments. Table 1 summarizes the frequencies of LIS hole features consisting of 1+ pixel, 2+ pixels, and 3+ pixels compared to the

353 number of LIS cluster features that contained large enough groups to potentially generate a 3+
354 pixel hole. LIS recorded 12 million large groups during the time period of interest, which
355 account for just 5% of all LIS groups. Only 0.37% of these large groups contain holes, and these
356 groups with holes occur in 0.84% of all flashes and 1.6% of all areas. Substantial holes that
357 encompass multiple pixels are considerably less frequent. Just 0.051% of large groups in 0.12%
358 of flashes and 0.24% of areas contain 3+ pixel holes. Group radiance anomalies that do not result
359 in holes (i.e., most of the panels in Figure 1) are not quantified in these fractions, but are
360 expected to occur at substantially higher frequencies.

361 To provide a sense of relative scale between the LIS hole features and their parent
362 groups, Figure 4 shows histograms of group size (Figure 4a), hole size (Figure 4b), and the ratio
363 between the two sizes (Figure 4c). Holes mostly occur in groups that consist of less than 50
364 pixels (Figure 4a), but holes are also noted in extraordinarily-large and presumably very bright
365 groups that contain hundreds of events. While 1-pixel holes are the most common (Figure 4b)
366 and account for 70% of the overall sample, larger holes even up to 29 pixels in size do exist.
367 Still, even in these truly exceptional holes cases, the hole features account for less than 42% of
368 the group footprint size – with most holes accounting for < 10%. Holes manifest as a portion of
369 the group missing, not generally as a thin ring of events surrounding an otherwise non-
370 illuminated center.

371 These hole features also occur throughout the TRMM domain. Figure 5 maps the
372 frequency of 1+ pixel LIS holes. To the first order, the hole distribution resembles the LIS/OTD
373 lighting climatology (Cecil et al., 2014) with hotspots in the tropical chimney regions of the
374 Americas, Africa, and the Maritime Continent in Asia. However, there are regional differences
375 that stand out. Hole features are particularly prominent in the southeastern United States, coastal

Central America, the Amazon, and eastern India, but are suppressed relative to the lightning climatology in the La Plata basin, and in northern India and Pakistan. These regional differences – most likely due to variations in thunderstorm organization, size, and structure – result in all three chimneys (Figure 4b) having nearly equal weights rather than the Africa dominance seen in the lightning climatology.

The four most active hole-producing regions (the southern United States, Central America / Colombia, the Congo Basin, and the Maritime Continent) are outlined in Figure 4 and the VIRS infrared brightness temperatures and PR near surface radar echoes coincident with the hole features in these regions are shown in Figure 5. To limit the potential for parallax and other pixel matching issues, we include only the larger hole features that contain at least three non-illuminated pixels. The PR near surface reflectivity parameter provides a measure of convective rigor and allows us to distinguish convection from overhanging anvil clouds (that lack PR echoes near the surface), while the VIRS infrared brightness temperature indicates the overall cloud-top height. The color contour shows the density of all LIS flashes in the mapped region, while the asterisk symbols denote the hole features. Co-located PR pixels that lack reflectivity are plotted along the y-axis. Dashed lines divide the figure domain according to whether the cloud regions have notable echoes near the surface (vertical line at 10 dBZ), whether the cloud-top brightness temperature is below freezing (horizontal line at 273 K), and whether the cloud-top temperature is below 235 K consistent with tall convective thunderstorms.

The overall lightning histograms (color contour) show that flashes illuminate a variety of cloud types in each mapped region including overhanging anvil clouds (top left box) and warm clouds / clear air regions that lack PR echoes (bottom left). This does not, necessarily, mean that these non-convective regions produce lightning. We examined the case of LIS flashes centered in

warm clouds previously, and found that these cases are located immediately adjacent to cold anvil shields that may be only partially illuminated by the flash (or not at all) – pushing their radiance-weighted centroids into warm clouds surrounding the thunderstorm (Peterson et al., 2017a).

Because we do not normalize by thunderstorm flash rate, both the overall flash histograms and the hole centroids are heavily weighted towards tall and intense convective clouds (top right). While the overall flash counts vary between regions, cloud types that produce holes are largely consistent across the global hotspots. Between 96% and 97% of holes in each region occur in tall stormclouds (VIRS CH4 IR Tb < 235 K) where convection (near surface PR echoes > 10 dBZ) accounts for 85% (Maritime Continent, Southern United States) to 89% (Colombia) of the holes, and overhanging anvil clouds (no PR echoes near the surface) accounts for the remaining 8-10%. Cold clouds that do not reach 235 K contain another 1-2% of the holes, while the remaining 0.5-1.5% are located in warm clouds. Plotting these warm cloud cases (not shown) reveals that these holes occur in breaks between thunderstorm features where the lightning can illuminate colder cloud regions on all sides of the hole.

3.3 Identifying Poorly-Transmissive Cloud Regions that do not Produce Holes in LIS Groups

While identifying holes in LIS groups can reveal clouds that block optical lightning emissions from reaching orbit, their rarity limits the practical utility of identifying them. A more general approach is needed that can identify poorly-transmissive clouds that might or might not produce holes. Such an algorithm adapted for real-time use could be leveraged to generate a gridded GLM product that alerts end users of the operational data to cloud regions that may have

reduced detection efficiency. This assessment would be based on how the clouds are being illuminated and thus not require ancillary data sources.

Our approach is based on the thundercloud imagery algorithm from Peterson (2019a). For every group that contains at least 8 events, we perform the following operations:

(1) Identify an approximate location for the emissions source for a given group
(2) Fit the radial function of event radiance to a mathematical model
(3) For every pixel within a specified radius of the source (whether it produced an event or not), compare the measured radiance with the model radiance for that radius
(4) Alert pixels that are significantly dimmer than predicted by the model as a radiance anomaly

Because this approach does not specify a restriction for long horizontal flashes, it is essentially assuming that these discharges are point source emitters at the spatial scale of LIS pixels. This is, of course, not true (Peterson, 2019b). However, finite source dimensions would only cause pixels far from the source location to have more energy than predicted by the model, not less. This would not generate false alarms, but it may cause some stratiform groups to be missed.

We previously used the location of peak event energy as the approximate position of the optical lightning source. This assumption is expected to be flawed in the types of clouds that we aim to identify. In many cases (i.e, in Figure 1), the brightest pixel is located within 1-2 pixels from the radiance anomaly. As these regions are often strong convection, it is anticipated that the lightning source is actually located within the anomaly and the brightest pixels occur where light is able to scatter through the side of the cloud. Rather than the brightest event location, we use the radiance-weighted group centroid location as an approximate position for the emissions source. If light escapes multiple sides of the poorly-transmissive cloud, then the centroid will be a more reasonable and stable approximation of the lightning source location than the location of

445 the single brightest pixel.

446 We further use a Gaussian function as the mathematical model in this application. We
447 assume that the normalized radiance of each pixel will decrease radially from its peak value at
448 the source location. However, the LIS group centroid locations are usually not aligned with the
449 event pixels, and - even when they are - the most radiant pixel can be offset from center. We thus
450 clamp the Gaussian function to the point (0 km, 100%), and force it to decrease from there.
451 Cases where the Gaussian fit fails are omitted from our analyses.

452 We define two tunable parameters that determine the conditions for alerted pixels. The
453 first of these is a radius of interest, within which we will consider non-illuminated LIS pixels
454 alongside the events. These pixels are assigned a normalized radiance of 0% and added to the
455 event list. This radius is currently chosen to equal the maximum event radius in the group minus
456 10 km (~2 pixels). For groups that are smaller than 10 km, no additional non-illuminated pixels
457 will be added. The second parameter is the alert flag threshold level – or, the maximum ratio of
458 measured to model radiance for a given pixel that will trigger an anomaly alert for the group in
459 question. Initial testing suggests that a threshold of ~20% is sufficient to identify poorly-
460 transmissive clouds without generating large numbers of false alarms.

461 We apply this algorithm to all LIS groups produced by the thunderstorm in Figures 1-3
462 that meet our minimum size criteria (at least 8 events). Figure 7 shows a case where the group in
463 question behaved as expected for a point-source emitter in a cloud with a simple geometry. The
464 group radiance pattern is plotted in Figure 7a using the same convention as Figure 1. The single
465 brightest pixel in the flash is located at the center of the 3x3 pixel box surrounding the flash,
466 while the surrounding pixels are relatively dim.

467 Figure 7b plots the radiance fall-off with distance for this group from its centroid

location. The black curve traces the measured event radiances with + symbols drawn at the event radii while the grey curve with diamond symbols depicts the Guassian fit at a 1-km interval. The group centroid was located ~2 km offset from the brightest pixel location (half a pixel), but the radiance otherwise fit the Gaussian model well. Because the group only illuminated one pixel on either side of the brightest pixel, the radius of interest is effectively zero and thus not shown.

Figure 7c quantifies how well the measurements fit the model by plotting the ratio between the measured and modeled radiance from each pixel. For all event pixels, the radiance ratio varied over a range that extended from 75% to 135%. No pixels fall below the 20% threshold. The non-illuminated pixel in the top-left of the group footprint in Figure 7a would have triggered an alert flag – except it fell outside the radius of interest. As a result, all pixels plotted in Figure 7d are either white (indicating pixels within the radius of interest with nominal status) or black (no data). Flagged events would be shaded grey if they existed for this group.

Figure 8 performs the same analysis on the 170-event group that contained the 3-pixel hole in Figure 1g. While the radiance of some of the events within the group decreases with radial distance in Figure 8b, there exists a collection of events at all distances that are among the least energetic in the group (close to the minimum threshold for detection). The two nearest events to the group centroid had only 32% and 11% of the maximum event energy, respectively, while the most radiant event was offset ~7 km from the group centroid.

Comparing the measured LIS radiance with the Gaussian model (Figure 8c) reveals a wide range of performance (as low as 0% to greater than 200%) across the group footprint. The Gaussian model struggles to represent the radiance pattern of this highly-irregular group. However, this is not due to random noise. If we plot the pixels that have < 20% of the model radiance from Figure 8c in Figure 8d (shaded grey), we find that they cluster in two specific

491 regions in the flash footprint: the radiance anomaly extending from the 3-pixel hole feature
492 eastward towards the most radiant pixel, and a line of non-illuminated pixels along the eastern
493 flank of group footprint that were within the radius of interest but did not trigger the instrument.
494 If desired, decreasing the radius of interest tunable parameter would remove the alerts at the edge
495 of the flash footprint.

496 Figure 9 collects alert flag counts from each group surveyed from the storm of interest on
497 the same grid used in Figure 2. The overall number of group anomaly alerts per gridpoint is
498 shown in Figure 9a. All of the alerted pixels are confined to either the anvil cloud on the western
499 flank of the storm or along the thunderstorm periphery to the north and east of the convective
500 core. We compare this alert count to the group count expressed as a Group Extent Density
501 (GED) in Figure 9b and find that the anvil cloud, at its peak, produced 9x more alerts than the
502 total number of groups that illuminated this region.

503 The alert flag counts and groups fractions in Figure 9a and b could form the basis for an
504 optical transmissivity stoplight product for space-based lightning imagers. Figure 9c and d
505 envision what such a product would look like by warning pixels that have multiple alerts and
506 marking pixels that have more alerts than groups with a fatal status. Warned pixels are indicated
507 in Figure 9c as white X symbols on top of the FED plot from Figure 2a, and fatal pixels are
508 indicated in the same way in Figure 9d. While the warned pixels extend over a large area
509 surrounding the anvil cloud on the western flank of the storm in Figure 9c, the only pixels in the
510 anvil cloud that are marked fatal are the 6 pixels with clearly depressed FED and TOE values in
511 Figure 2. Additionally, two fatal pixels are identified on the eastern flank of the illuminated
512 storm feature outside of the convective core.

513 This algorithm provides confirmation that the qualitative indicators of a possible

514 reduction of DE (suppressed TOE and FED values within the overall illuminated cloud feature)
515 are, in fact, caused by anomalies in the underlying group radiance patterns that correspond to
516 poor transmission, making it a strong candidate for further development.
517

518 **4 Conclusion**

519 In this study, we examine how clouds are illuminated during individual LIS groups in
520 order to identify radiance anomalies consistent with poorly-transmissive cloud regions. Certain
521 clouds block light from reaching orbit and triggering instruments like LIS. Such regions manifest
522 as LIS pixels that remain dark even when surrounded by bright pixels, and they are particularly
523 evident in the largest LIS groups. A special case of this kind of radiance anomaly is when certain
524 pixels within the LIS group footprint fail to trigger, resulting in a hole of non-illuminated pixels
525 completely encompassed by events. Holes can be simply identified by adapting a similar
526 technique for clustering LIS events into groups – except searching for contiguous dark regions in
527 the middle of illuminated pixels rather than contiguous illuminated pixels on the otherwise-dark
528 CCD imaging array.

529 We identify 44,829 cases of LIS holes in the TRMM-LIS record. PR, TMI, and VIRS
530 observations coincident with hole centroids indicate that they occur primarily in (1) tall, vigorous
531 convection (87%) and (2) anvil clouds that lack PR echoes near the surface (10%). We attempt to
532 identify general cases of group radiance anomalies (not just holes) by comparing the radiance
533 fall-off with distance for individual large LIS groups with a Gaussian model. Pixels whose
534 measured energies are substantially lower (< 20%) than the radiance expected by the model
535 given their locations are alerted. Alerts from every large groups (at least 8 pixels) are then
536 accumulated on a 5-km grid over the thunderstorm. Regions that block optical transmission are

alerted multiple times over the instrument view time (flagged as a warning status), while certain regions accumulated more alerts than there were actual groups illuminating the cloud (flagged as a fatal status). Comparing these warning / fatal status flags with standard gridded products (FED, TOE) provides an explanation for why these grids are depressed in certain storm regions – poor optical transmission. This analysis demonstrates what a future optical transmission stoplight product might look like for GLM.

Acknowledgments

This work was supported by the US Department of Energy through the Los Alamos National Laboratory (LANL) Laboratory Directed Research and Development (LDRD) program under project number 20200529ECR. Los Alamos National Laboratory is operated by Triad National Security, LLC, for the National Nuclear Security Administration of U.S. Department of Energy (Contract No. 89233218CNA000001). The TRMM LIS data used in this work may be accessed via the NASA Global Hydrology Resource Center DAAC, while the multi-sensor TRMM 1Z09 data are hosted at Texas A&M University Corpus Christi (http://atmos.tamucc.edu/trmm/data/trmm/level_1/).

References

Bateman, M. and D. M. Mach, (2020): Preliminary detection efficiency and false alarm rate assessment of the Geostationary Lightning Mapper on the GOES-16 satellite. *J. Appl. Rem. Sens.* **14**(3) 032406 (17 April 2020) https://doi.org/10.1117/1.JRS.14.032406

Bitzer, P. M., 2019: The fruit basket of GLM detection efficiency. *GLM Science Team Meeting, 2019.* Huntsville, AL, USA, 33 slides. Available online at: https://goes-r.nsstc.nasa.gov/home/sites/default/files/2019-09/Bitzer_20190912_glm_sci_mtg.pptx.

Blakeslee, R. J., H. J. Christian, M.F. Stewart, D.M. Mach, M. Bateman, T.D. Walker, D. Buechler, W.J. Koshak, S. O'Brien, T. Wilson, E.C. Colley, T. Abbott, J. Carter S. Pavelitz, C. Coker, 2014: Lightning Imaging Sensor (LIS) for the International Space Station (ICC): Mission description and science goals, *XV Int. Conf. Atmos. Electricity.* Norman, OK, 15pp.

564 Bruning, E.C. and D.R. MacGorman, 2013: Theory and Observations of Controls on Lightning
565 Flash Size Spectra. *J. Atmos. Sci.,* **70**, 4012–4029, https://doi.org/10.1175/JAS-D-12-
566 0289.1
567 Bruning, E., Tillier, C. E., Edgington, S. F., Rudlosky, S. D., Zajic, J., Gravelle, C., et al. (2019).
568 Meteorological imagery for the geostationary lightning mapper. *Journal of Geophysical*
569 *Research: Atmospheres*, 2019; 124: 14285– 14309.
570 https://doi.org/10.1029/2019JD030874
571 Cecil, D. J., Buechler, D. E., & Blakeslee, R. J. (2014). Gridded lightning climatology from
572 TRMM-LIS and OTD: Dataset description. *Atmospheric Research*, ***135***, 404-414.
573 Cecil, D.J. and T. Chronis, 2018: Polarization-Corrected Temperatures for 10-, 19-, 37-, and 89-
574 GHz Passive Microwave Frequencies. *J. Appl. Meteor. Climatol.,* **57**, 2249–2265,
575 https://doi.org/10.1175/JAMC-D-18-0022.1
576 Christian, H.J., R.L. Frost, P.H. Gillaspy, S.J. Goodman, O.H. Vaughan, M. Brook, B. Vonnegut,
577 and R.E. Orville, 1983: Observations of Optical Lightning Emissions from above
578 Thunderstorms Using U-2 Aircraft. *Bull. Amer. Meteor. Soc.,* **64**, 120–123,
579 https://doi.org/10.1175/1520-0477(1983)064<0120:OOOLEF>2.0.CO;2
580 Christian, H.J. and S.J. Goodman, 1987: Optical Observations of Lightning from a High-Altitude
581 Airplane. *J. Atmos. Oceanic Technol.,* **4**, 701–711, https://doi.org/10.1175/1520-
582 0426(1987)004<0701:OOOLFA>2.0.CO;2
583 Christian, H. J., R. J. Blakeslee, S. J. Goodman, and D. M. Mach (Eds.), 2000: Algorithm
584 Theoretical Basis Document (ATBD) for the Lightning Imaging Sensor (LIS),
585 NASA/Marshall Space Flight Center, Alabama. (Available as
586 http://eospso.gsfc.nasa.gov/atbd/listables.html, posted 1 Feb. 2000)
587 Goodman, S. J., D. Mach, W. J. Koshak, and R. J. Blakeslee. (2010). *GLM Lightning Cluster-*
588 *Filter Algorithm (LCFA) Algorithm Theoretical Basis Document (ATBD)*. Retrieved from
589 https://www.goes-r.gov/products/ATBDs/baseline/Lightning_v2.0_no_color.pdf, posted
590 24 Sept. 2010
591 Koshak, W. J., Solakiewicz, R. J., Phanord, D. D., and Blakeslee, R. J. (1994), Diffusion model
592 for lightning radiative transfer, *J. Geophys. Res.*, 99(D7), 14361– 14371,
593 doi:10.1029/94JD00022.
594 Koshak, W. J., 2010: Optical characteristics of OTD flashes and the implications for flash-type
595 discrimination. *J. Atmos. Oceanic. Technol.,* **27,** 1,822 – 1,838
596 Kummerow, C., Barnes, W., Kozu, T., Shiue, J., & Simpson, J. (1998). The Tropical Rainfall
597 Measuring Mission (TRMM) Sensor Package. *Journal of Atmospheric and Oceanic*
598 *Technology, 15*(3), 809-817. doi:10.1175/1520-0426(1998)015<0809:Ttrmmt>2.0.Co;2
599 Light, T. E., Suszcynsky, D. M., Kirkland, M. W., and Jacobson, A. R. (2001a), Simulations of
600 lightning optical waveforms as seen through clouds by satellites, *J. Geophys. Res.*, 106(
601 D15), 17103– 17114, doi:10.1029/2001JD900051.
602 Light, T. E., Suszcynsky, D. M., and Jacobson, A. R. (2001b), Coincident radio frequency and
603 optical emissions from lightning, observed with the FORTE satellite, *J. Geophys. Res.*,
604 106(D22), 28223– 28231, doi:10.1029/2001JD000727.
605 Liu, C., E.J. Zipser, D.J. Cecil, S.W. Nesbitt, and S. Sherwood, 2008: A Cloud and Precipitation
606 Feature Database from Nine Years of TRMM Observations. *J. Appl. Meteor. Climatol.,*
607 **47**, 2712–2728, https://doi.org/10.1175/2008JAMC1890.1

608 Lojou, J.-Y., & Cummins, K. L. (2004). On the representation of two- and three-dimensional
609 total lightning information. *In Preprints, Conference on Meteorological Applications of*
610 *Lightning Data*, Paper 2.4, AMS Annual Meeting, San Diego, CA, USA.
611 Mach, D. M., Christian, H. J., Blakeslee, R. J., Boccippio, D. J., Goodman, S. J., & Boeck, W. L.
612 (2007). Performance assessment of the Optical Transient Detector and Lightning Imaging
613 Sensor. *Journal of Geophysical Research: Atmospheres, 112*(D9).
614 doi:10.1029/2006jd007787
615 Peterson, M., and Liu, C. (2013), Characteristics of lightning flashes with exceptional
616 illuminated areas, durations, and optical powers and surrounding storm properties in the
617 tropics and inner subtropics, *J. Geophys. Res. Atmos.*, 118, 11,727– 11,740,
618 doi:10.1002/jgrd.50715.
619 Peterson, M., Deierling, W., Liu, C., Mach, D., and Kalb, C. (2017a), The properties of optical
620 lightning flashes and the clouds they illuminate, *J. Geophys. Res. Atmos.*, 122, 423– 442,
621 doi:10.1002/2016JD025312.
622 Peterson, M., Rudlosky, S., & Deierling, W. (2017b). The evolution and structure of extreme
623 optical lightning flashes. *Journal of Geophysical Research: Atmospheres*, 122, 13,370–
624 13,386. https://doi.org/10.1002/2017JD026855
625 Peterson, M., Rudlosky, S., & Deierling, W. (2018). Mapping the lateral development of
626 lightning flashes from orbit. *Journal of Geophysical Research: Atmospheres*, 123, 9674–
627 9687. https://doi.org/10.1029/2018JD028583
628 Peterson, M., & Rudlosky, S. (2019). The time evolution of optical lightning flashes. *Journal of*
629 *Geophysical Research: Atmospheres*, 124, 333– 349.
630 https://doi.org/10.1029/2018JD028741
631 Peterson, M. (2019a). Using lightning flashes to image thunderclouds. *Journal of Geophysical*
632 *Research: Atmospheres*, 124, 10175– 10185. https://doi.org/10.1029/2019JD031055
633 Peterson, M. (2019b). Research applications for the Geostationary Lightning Mapper
634 operational lightning flash data product. *Journal of Geophysical Research: Atmospheres*,
635 124, 10205– 10231. https://doi.org/10.1029/2019JD031054
636 Rudlosky, S. D., Goodman, S. J., Virts, K. S., & Bruning, E. C. (2019). Initial Geostationary
637 Lightning Mapper Observations. *Geophysical Research Letters, 46*(2), 1097-1104.
638 doi:10.1029/2018gl081052
639 Rutledge, S. A., K. Hilburn, A. Clayton, & B. Fuchs, 2019: CSU GLM work summary. *GLM*
640 *Science Team Meeting, 2019.* Huntsville, AL, USA, 20 slides. Available online at:
641 https://goes-r.nsstc.nasa.gov/home/sites/default/files/2019-
642 09/GLM%20presentation%20Sept%202019_FINAL.pptx.
643 Said, R., & M. Murphey, 2019: Spatiotemporal patterns of GLM flash DE. *GLM Science Team*
644 *Meeting, 2019.* Huntsville, AL, USA, 18 slides. Available online at: https://goes-
645 r.nsstc.nasa.gov/home/sites/default/files/2019-09/Said_GLM_2019.pptx.
646 Spencer, R.W., H.M. Goodman, and R.E. Hood, 1989: Precipitation Retrieval over Land and
647 Ocean with the SSM/I: Identification and Characteristics of the Scattering Signal. *J.*
648 *Atmos. Oceanic Technol.,* **6**, 254–273, https://doi.org/10.1175/1520-
649 0426(1989)006<0254:PROLAO>2.0.CO;2
650 Suszcynsky, D. M., Kirkland, M. W., Jacobson, A. R., Franz, R. C., Knox, S. O., Guillen, J. L.
651 L., and Green, J. L. (2000), FORTE observations of simultaneous VHF and optical
652 emissions from lightning: Basic phenomenology, *J. Geophys. Res.*, 105(D2), 2191–
653 2201, doi:10.1029/1999JD900993.

Suszcynsky, D. M., Light, T. E., Davis, S., Green, J. L., Guillen, J. L. L., and Myre, W. (2001), Coordinated observations of optical lightning from space using the FORTE photodiode detector and CCD imager, *J. Geophys. Res.*, 106(D16), 17897– 17906, doi:10.1029/2001JD900199.

Thomas, R., P.R. Krehbiel, W. Rison, T. Hamlin, D. J. Boccippio, S. J. Goodman, and H. J. Christian, 2000: Comparison of ground-based 3-dimensional lightning mapping observations with satellite-based LIS observations in Oklahoma. *Geophys. Res. Lett.*, **27**, 12, 1,703-1,706.

Thomas, R., 2019: Low GLM detection efficiencies in large storms. *GLM Science Team Meeting, 2019.* Huntsville, AL, USA, 18 slides. Available online at: https://goes-r.nsstc.nasa.gov/home/sites/default/files/2019-09/Thomas-GLM-sci-meeting-2019.pdf.

Thomson, L.W. and E.P. Krider, 1982: The Effects of Clouds on the Light Produced by Lightning. *J. Atmos. Sci.,* **39**, 2051–2065, https://doi.org/10.1175/1520-0469(1982)039<2051:TEOCOT>2.0.CO;2

Toracinta, E.R., D.J. Cecil, E.J. Zipser, and S.W. Nesbitt, 2002: Radar, Passive Microwave, and Lightning Characteristics of Precipitating Systems in the Tropics. *Mon. Wea. Rev.,* **130**, 802–824, https://doi.org/10.1175/1520-0493(2002)130<0802:RPMALC>2.0.CO;2

Vonnegut, B., O.H. Vaughan, M. Brook, and P. Krehbiel, 1985: Mesoscale Observations of Lightning from Space Shuttle. *Bull. Amer. Meteor. Soc.,* **66**, 20–29, https://doi.org/10.1175/1520-0477(1985)066<0020:MOOLFS>2.0.CO;2

Zhang, D., & Cummins, K. L. (2020). Time evolution of satellite-based optical properties in lightning flashes, and its impact on GLM flash detection. *Journal of Geophysical Research: Atmospheres*, 125, e2019JD032024. https://doi.org/10.1029/2019JD032024

688 **Table 1.** Frequencies of hole features in the TRMM record and LIS lightning with suitibly-large
689 groups for possibly generating holes. Multi-pixel hole features are exceptionally rare in the LIS
690 data.
691

	Large (≥14 Pixel) Groups	Unique Flashes with Large Groups	Unique Areas with Large Groups
LIS Lightning	12,156,986	4,550,182	2,200,219
1+ Pixel Holes	0.37%	0.84%	1.6%
2+ Pixel Holes	0.058%	0.14%	0.29%
3+ Pixel Holes	0.051%	0.12%	0.24%

692
693

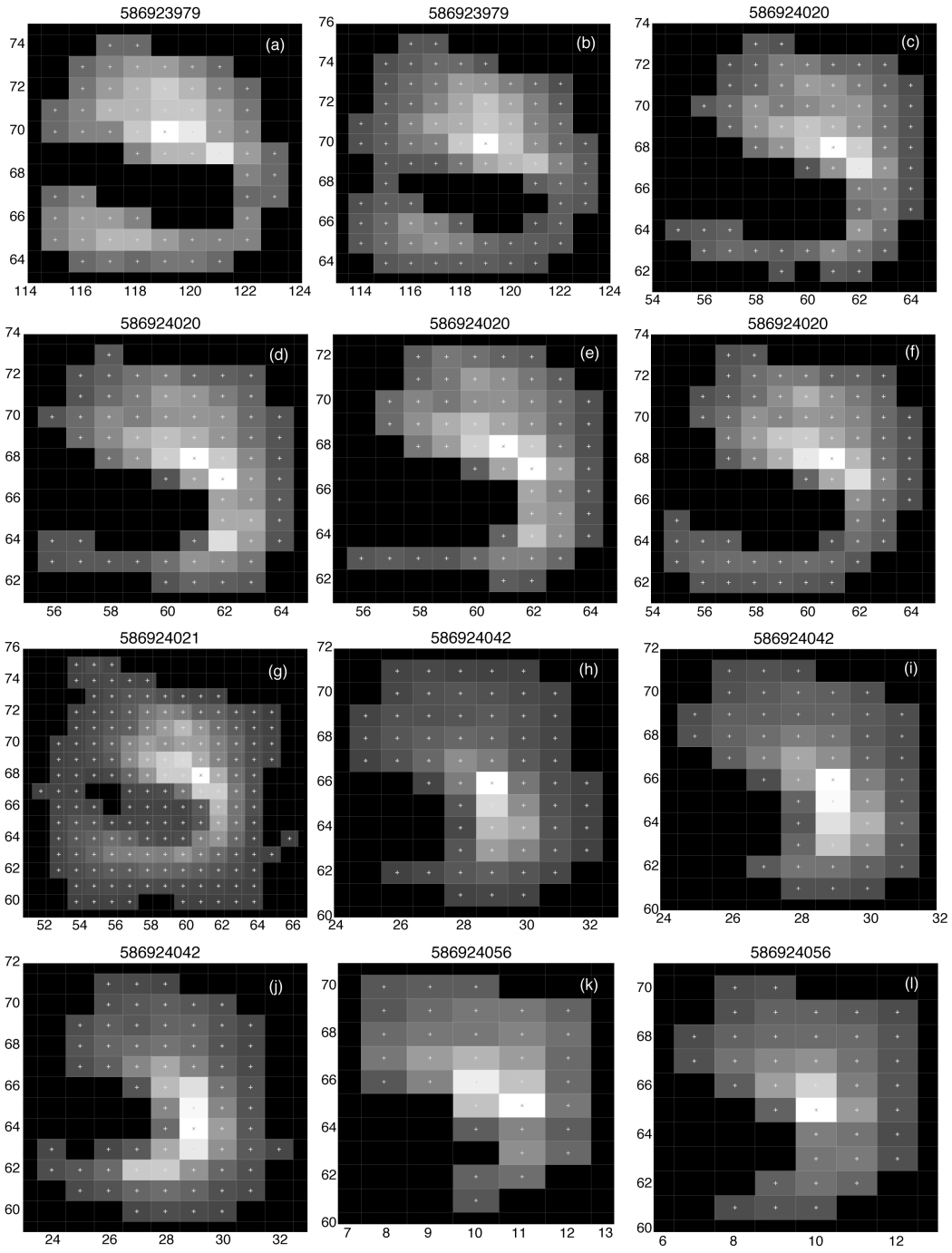

Figure 1. Twelve large LIS groups that illuminate the same storm region over a ~77 s period with similar radiance anomalies present in their footprints. X and Y coordinates are positions on the LIS CCD array. Pixels are colored according to normalized brightness with the most radiant pixel shaded white (with an asterisk symbol at its center) and less-radiant pixels shaded darker grey (with + symbols at their centers). Black pixels did not produce events during the group. Panel titles indicate the whole-second TAI93 count for the group in question.

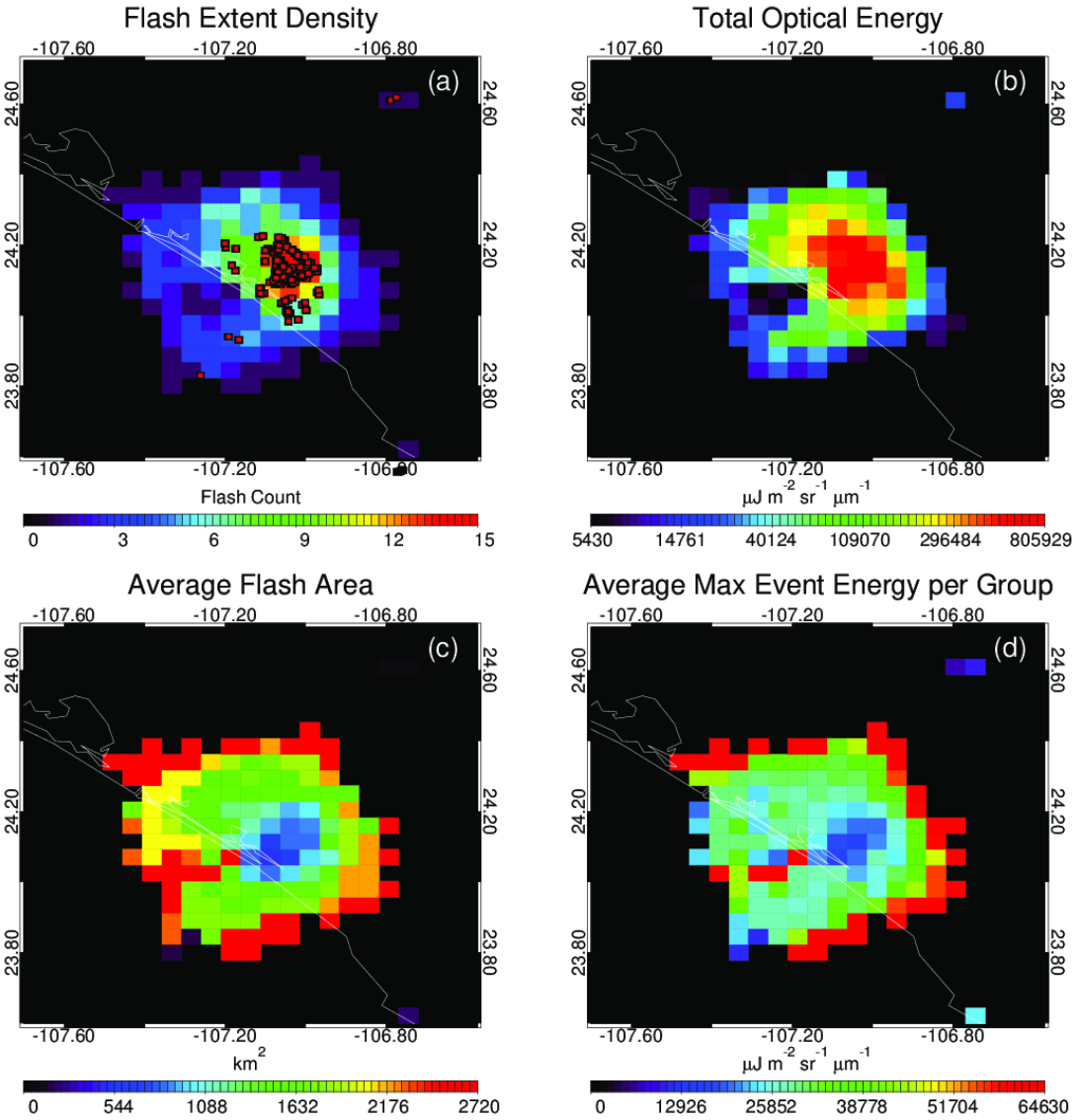

Figure 2. Meteorological LIS imagery of a thunderstorm over Sinaloa, Mexico that contains multiple LIS holes. (a) Flash Extent Density with group centroid overlaid with red box symbols. (b) Total Optical Energy. (c) Average Flash Area. (d) The average radiance of the brightest event in each group that illuminates each gridpoint. The poorly-transmissive cloud responsible for the holes has reduced FED and TOE values with increased AFA and average maximum event energies.

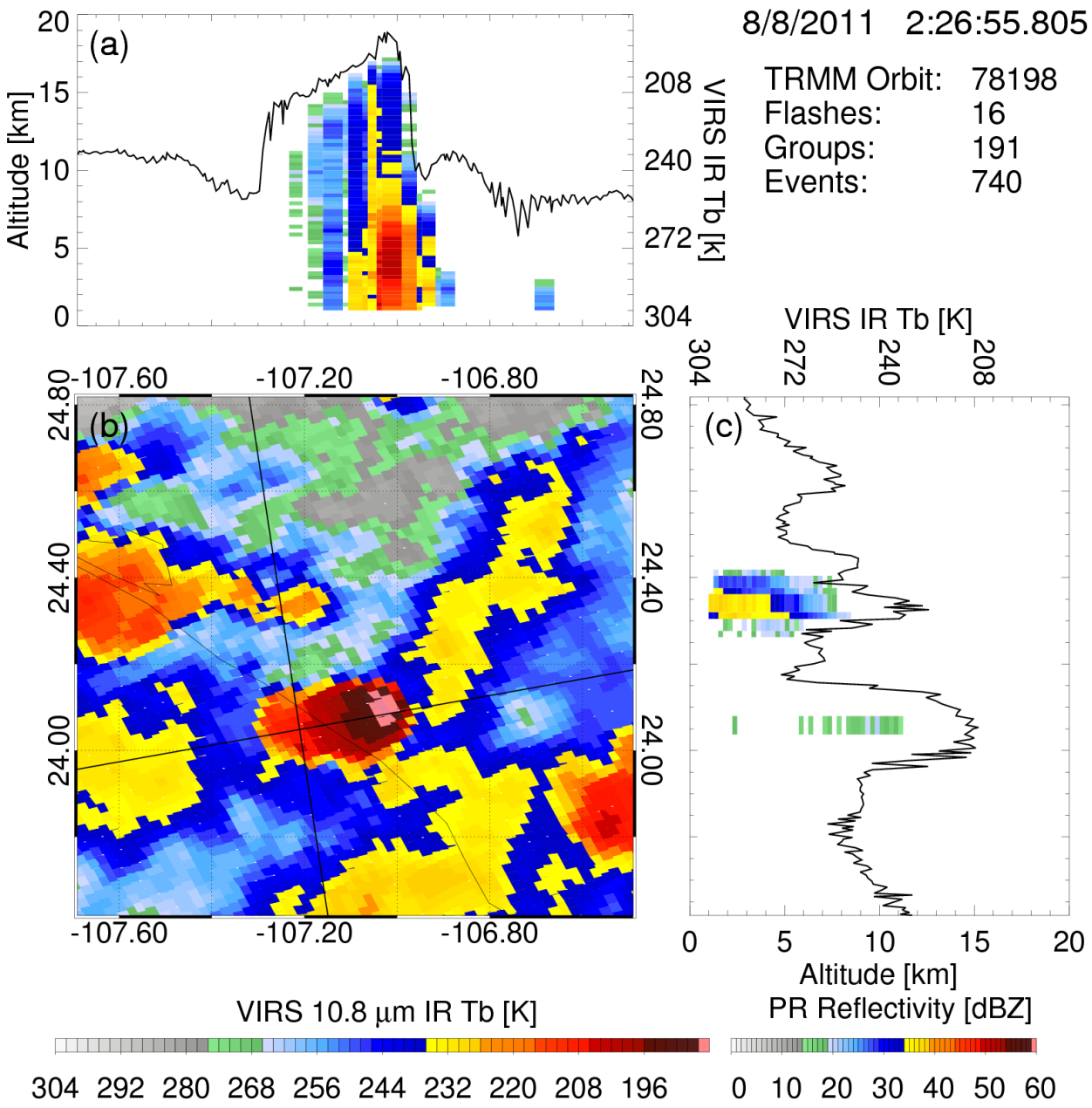

Figure 3. TRMM VIRS and PR imagery of the same storm from Figure 2. The VIRS CH4 (10.8 µm) infrared brightness temperatures are shown as a plan view in (b) with solid lines corresponding to the quasi-meridional (a) and quasi-zonal (c) PR and VIRS cross sections shown in the outer panels.

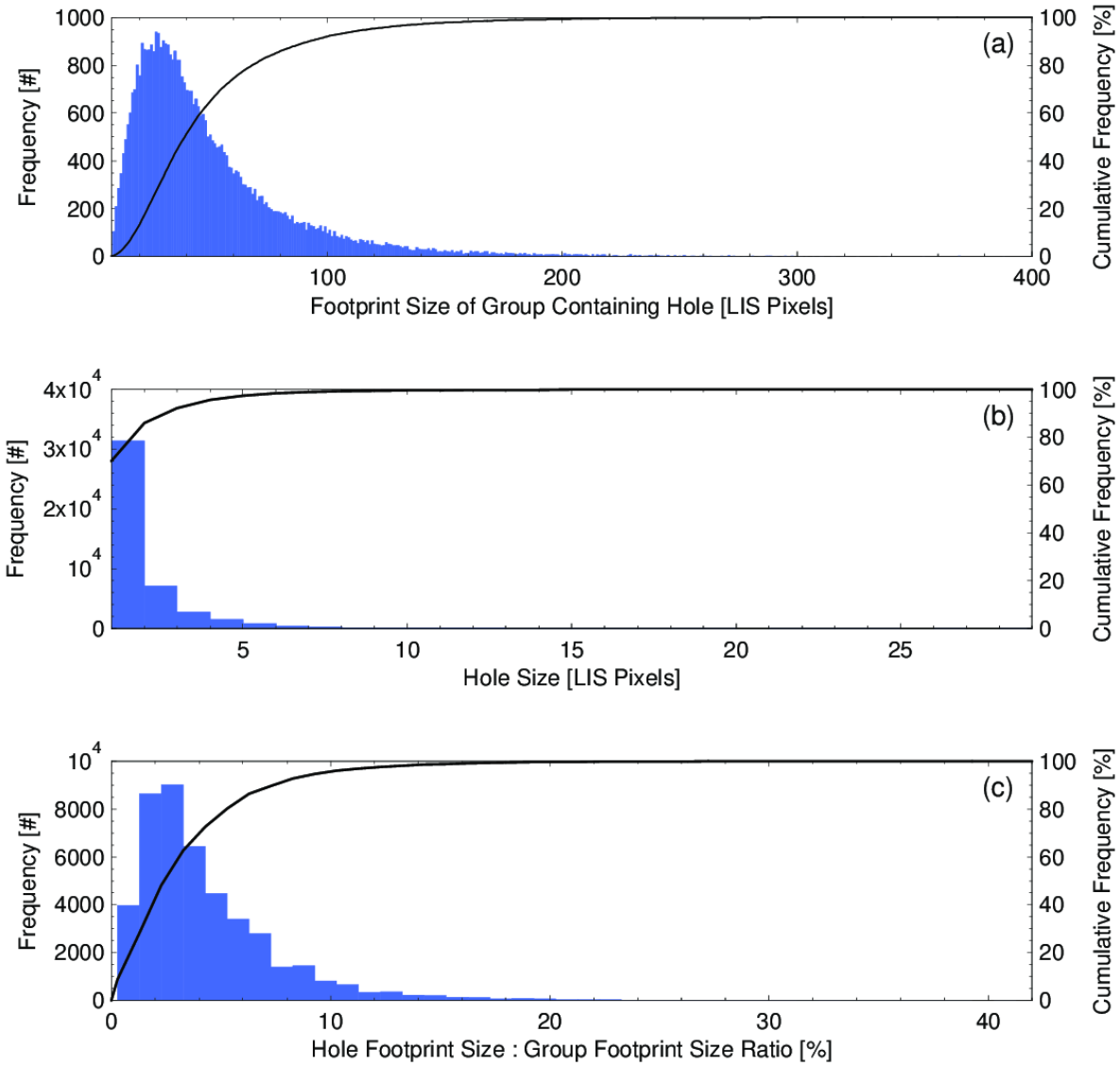

Figure 4. Histograms (blue bars) and Cumulative Distribution Functions (CFDs: solid lines) for (a) the sizes of LIS groups that produce holes, (b) the size of hole features, and (c) the ratio of the size of the hole to the size of the parent group. Even the largest holes are small compared to the surrounding LIS group.

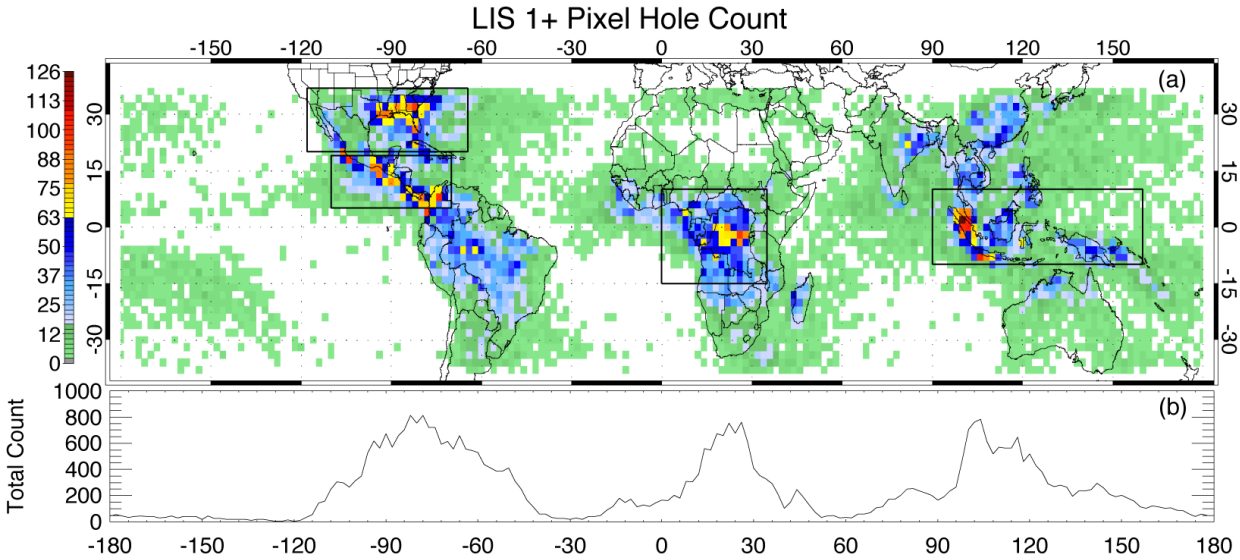

Figure 5. Global distribution (a) and total count by longitude (b) of LIS hole features. The four most active regions for producing holes (southern United States, Central America / Colombia, the Congo Basin, and the Maritime Continent) are outlined with solid boxes.

729

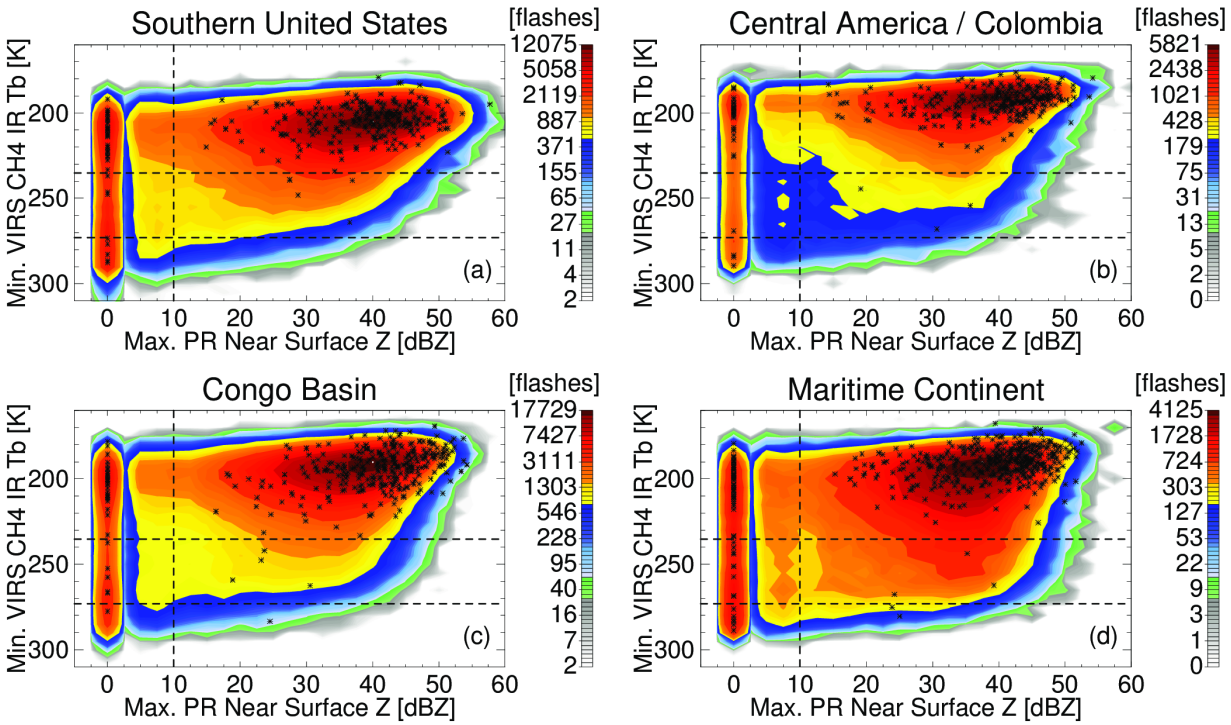

730

731 **Figure 6.** Two-dimensional histograms of the PR near surface reflectivities and VIRS CH4
732 infrared brightness temperatures at the centroid location of LIS flashes in (a) the Southern United
733 States, (b) Central America / Colombia, (c) the Congo Basin, and (d) the Maritime Continent. PR
734 / VIRS measurements at hole centroids are plotted as asterisk symbols.

735

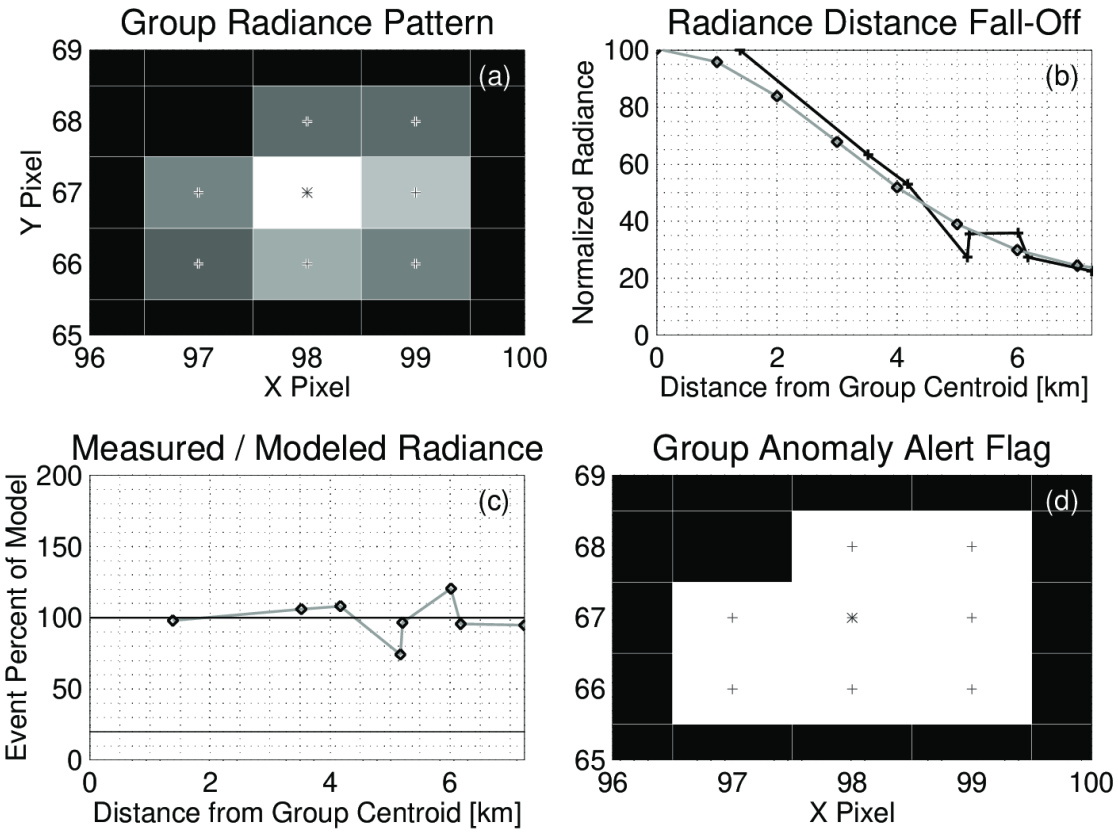

Figure 7. The spatial radiance distribution of an 8-pixel LIS group. (a) The radiance pattern following the convention of Figure 1. (b) The normalized radiance of LIS groups (+ symbols connected with black lines) as a function of distance from the group centroid location. A Gaussian fit to the data is plotted as a grey curve with diamond symbols. (c) The fraction of the radiance form the Gaussian model that is measured by LIS in each pixel with the 20% alert threshold shown as a solid horizontal line. (d) The alert flag status of each pixel where white indicated nominal and grey indicates an alert. There are no alerted pixels in this group because all pixels conform well to the model.

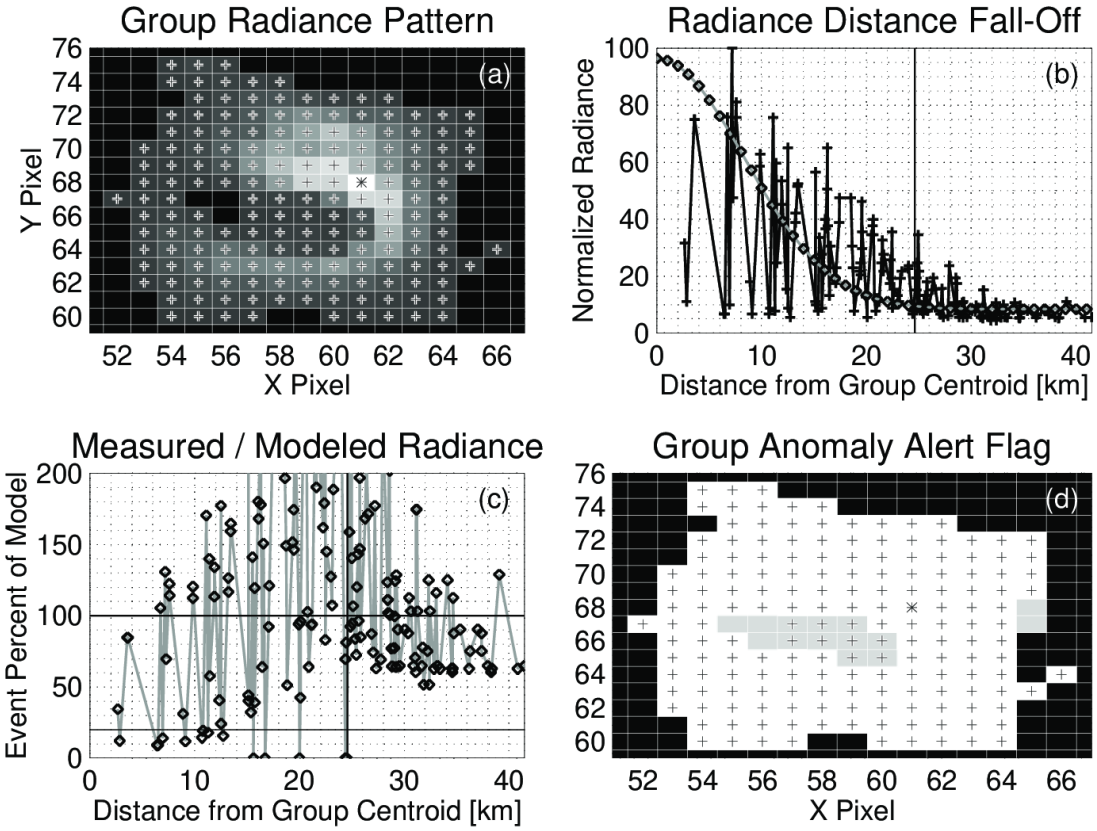

Figure 8. As in Figure 7, but for a large (170 pixel) LIS group with a 3-pixel hole. The vertical line in (b) indicates the radius of interest within which non-illuminated pixels will be considered alongside events in (c) and (d). 14 pixels are alerted in this case – all but two are located in the notably dim center of the flash from (a).

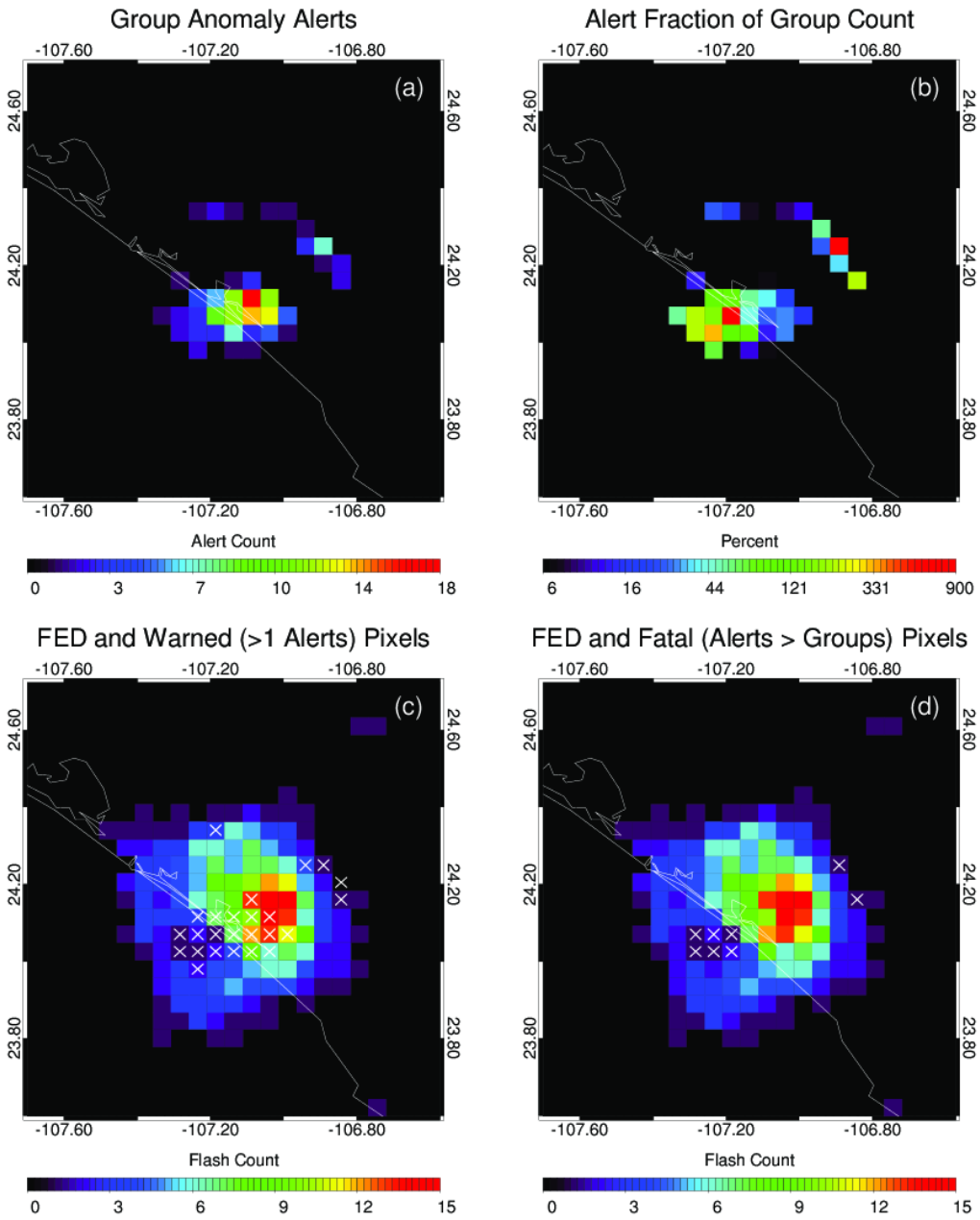

Figure 9. Pixel-level group radiance anomaly alert flags are integrated on the same grid used to create the meteorological imagery in Figure 2. Alert counts (a) are concentrated to the west of the convective core where they can outnumber the group illuminating that region (b). A prototype stoplight product might warn on gridpoints with multiple alerts and set a fatal status for pixels that have more alerts than groups. (c) and (d) visualize such warned and fatal pixels as white X symbols on top of FED imagery.